Joint one-dimensional inversion of magnetotelluric data and surface-wave dispersion curves using correspondence maps

M. Aquino, Guy Marquis, J. Vergne

Geophysical Prospecting

EAGE EUROPEAN ASSOCIATION OF GEOSCIENTISTS & ENGINEERS

Geophysical Prospecting, 2022, **70**, 1455–1470 doi: 10.1111/1365-2478.13239

Joint one-dimensional inversion of magnetotelluric data and surface-wave dispersion curves using correspondence maps

M. Aquino*, G. Marquis and J. Vergne

CNRS, ENGEES, Institut Terre et Environnement de Strasbourg, Université de Strasbourg, UMR 7063, 5 rue Descartes, Strasbourg, F-67084, France

Received May 2021, revision accepted May 2022

ABSTRACT

We use a correspondence map to jointly invert surface-wave dispersion curves and magnetotelluric data for subsurface shear velocity and resistivity but also for a possible relationship between them. Our first experiments consist of inversions of synthetic data computed from models linked by first- and second-order polynomial relationships. Our methodology produces joint inversion model pairs from which 100% fit the 'observed' parameter relationship within a 5% error vs only 15% of the separate inversion pairs for the degree 1 relationship experiment. For the degree 2 relationship synthetic test, 80% of the joint inversion model pairs fit the 'observed' relationship within a 5% error while 45% of the separate inversion pairs. This reduces the number of acceptable models without compromising the data fit ('reduction of non-uniqueness'). The next experiment involves synthetic data from models of known physical properties, taken from well logs, but without a known relationship. We show how to select an appropriate polynomial degree for joint inversion when the relationship is unknown. Having validated the approach with synthetic cases, we apply our methodology to field data. We compare separate and joint inversions, and we find that the one-dimensional subsurface models retrieved from joint inversions are more similar to previous models documented in the area than the separate inversion models.

Key words: Passive methods, magnetotelluric, ambient seismic noise, joint inversion, correspondence maps.

INTRODUCTION

Joint inversion of geophysical data has been proposed as a means for understanding subsurface structures, since taking advantage of different data sensitivities can reduce the range of acceptable models (i.e. the 'non-uniqueness') (Moorkamp *et al.*, 2007). One can implement joint inversion in many different ways: (1) joint inversion for a single physical property from multiple datasets is sensitive to it, for example apparent resistivity from DC resistivity and magnetotelluric data (Jupp and Vozoff, 1975) or shear velocity from receiver functions with surface wave dispersion curves (Julià *et al.*, 2000); and (2) joint inversion of data sensitive to different physical parameters, for example resistivity and seismic velocity (Gallardo and Meju, 2003). For the first type, the joint inversion procedure is straightforward as both methods share a common subsurface model. The second type, however, is more challenging since sensing different physical properties involves questions about their mutual coupling (or lack thereof). Here we focus on the second type of joint inversion to obtain shear-wave velocity and electrical resistivity models from surface-wave dispersion curves and magnetotelluric data, respectively. The core element of any joint inversion methodology is, therefore, the hypothesis of a link between the different physical property

The paper was presented at the 82nd EAGE Conference & Exhibition, Amsterdam, the Netherlands.

*E-mail: monicaquino92@gmail.com

models (Carrillo and Gallardo, 2018). In general, these links or features can be classified as structural or petrophysical.

Structurally coupled joint inversion assumes that different geophysical methods sense the same underlying geology; therefore, it is the structure that controls the distribution of petrophysical properties (Gallardo and Meju, 2003). With this approach, the structural similarity of the different physical property models is considered rather than petrophysical relationships between these properties. They require the specification of mathematical conditions at structural boundaries in a numerically stable way. Today, the most common structural coupling method is the cross-gradient constraint, introduced by Gallardo and Meju (2003, 2004) and for which the structural similarity is enforced by minimizing the magnitude of the cross-gradient vector. Other structural constraints include either curvature-based methods, for example Zhang and Morgan (1997) and Haber and Oldenburg (1997), or Gramian constraints, for example Zhdanov *et al.* (2012) and Ogunbo and Shin (2021).

Structural coupling does not make any assumption about the petrophysical relationships between the parameters. If there is a priori information about such relationships, joint inversion results can be improved significantly. Hence, structural coupling might overlook the full potential of the joint inversion (Moorkamp, 2017). Joint inversion methods using parameter relationships are based on the fact that for some specific geological environments geophysical parameters can be related to some mathematical relationships. Carcione *et al.* (2007) showed how in sedimentary environments porosity and fluids of the rock matrix can provide a physical link that causes a correlation between seismic velocities and electrical conductivities. The so-called petrophysical joint inversion has generally been approached in two ways: (1) when there is a relationship between the parameters which are used to constrain the dependent parameters, in a sequential inversion mode, for example Dufréchou *et al.* (2018) and Gautier *et al.* (2019) and (2) when the parameter relationship is included as part of the joint inversion workflow. From this second group, Tiberi *et al.* (2008) retrieved linear relationships with the depth between the density and the compressional velocity in a Birch (1960) type relationship. Carrillo and Gallardo (2018) proposed a way to retrieve higher order polynomial relationships for a number of heterogeneous zones.

We present here a joint inversion methodology that includes the correspondence map approach described by Carrillo and Gallardo (2018), implemented as an Occam-type inversion (Constable *et al.*, 1987). Our approach, in addition to inverting the data using geometric constraints, seeks a functional relationship simultaneously for any pair of model parameters. The relationship is treated as a random variable as part of the joint inversion algorithm. Carrillo and Gallardo (2018) propose a general form of the relationship between two model parameters ($\mathbf{m}_1$ and $\mathbf{m}_2$): p and q are the maximum power allowed for each parameter, and a_{ij} are the polynomial coefficients linking $\mathbf{m}_1$ and $\mathbf{m}_2$. They introduce the function g:

$$g(\mathbf{m}_1, \mathbf{m}_2, a) = \sum_{i=0}^{q} \sum_{j=0}^{p} a_{ij} \mathbf{m}_1^i \mathbf{m}_2^j = 0. \tag{1}$$

Our work focuses on exploring the use of correspondence maps to invert for the one-dimensional shear velocity from dispersion curve data (from ambient seismic noise) and the resistivity (from magnetotelluric data). We first illustrate the method of synthetic data using linear (polynomial of degree 1) and non-linear relationships (polynomial of degree higher than 1). We then apply our methodology to field data. Throughout the paper, we use the same notation as Carrillo and Gallardo (2018) and Constable *et al.* (1987) to help the reader to relate our work to these seminal articles.

DATASETS

Magnetotelluric data

Magnetotellurics (MT) is one of the most widely used geophysical methods to obtain the Earth's subsurface resistivity structures. The principle of MT is to acquire simultaneous measurements of the horizontal components of the electric field $\mathbf{E}$ and the magnetic field $\mathbf{H}$ at the Earth's surface. In the Fourier domain, the transfer function between these components of $\mathbf{E}$ and $\mathbf{H}$ yields the complex impedance tensor $\mathbf{Z}$ from which the apparent resistivity ρ_a and phase ϕ_a can be computed:

$$\mathbf{E}(\omega) = \mathbf{Z}(\omega)\mathbf{H}(\omega), \tag{2}$$

$$\rho_a(\omega) = \frac{|\mathbf{Z}(\omega)|^2}{\mu\omega}, \ \phi_a(\omega) = \arg \mathbf{Z}(\omega), \tag{3}$$

where ω is the angular frequency (i.e. $2\pi f$) and μ is the magnetic permeability. The impedance tensor is frequency dependent, the impedances at high frequencies correspond to shallow structures, while impedances at low frequencies correspond to deeper structures. The reader is referred to Vozoff (1990) for more details about MT.

We calculate synthetic impedances for a one-dimensional isotropic layered earth by computing the effective impedance at the surface of the Earth using the recursive approach

described in, for example, Ward and Hohmann (2012). To ensure stability and avoid negative values of resistivity during the inversion process, we use the natural logarithm of ρ as inversion parameters in all our computations.

Rayleigh wave dispersion data from ambient seismic noise correlation

For many events in a seismic record, the surface waves are the largest amplitude feature present in the seismogram. Surface Rayleigh waves are the result of interfering P-Sv waves. Particle motion of the fundamental mode of Rayleigh waves moving from left to right is elliptical in a retrograde (counterclockwise) direction. The motion is constrained to the vertical plane that is consistent with the direction of the wave propagation (Xia *et al.*, 1999). Surface waves are guided and dispersive. Just as is the case for the electromagnetic waves in MT, lower frequencies penetrate deeper than higher frequencies for a given mode. Analysis of the kernels of surface wave dispersion curves shows that they are primarily sensitive to shear wave velocity variations and less sensitive to compressional velocity and density (Dorman and Ewing, 1962; Xia *et al.*, 1999; Julià *et al.*, 2000; Song *et al.*, 2005).

Commonly, subsurface reservoir imaging is based on active seismic sources, but more recently the cross-correlations of ambient seismic noise records have shown the capability of empirically obtaining Green's function between a pair of receivers (Shapiro *et al.*, 2005), which has become a standard technique for passive seismic imaging. In this paper, we invert only for shear wave velocity and compute compressional velocity from a given V_p/V_s ratio. The forward computation of dispersion curves is done using the *disba* python library (Luu, 2019), which is based on the code *sdisp96* from *Computer Programs in Seismology* (Herrmann, 2013). Similar to MT data and resistivity models, we use the natural logarithm of shear velocity in all computations for inversion.

JOINT INVERSION METHOD

We have chosen Occam's inversion method (Constable *et al.*, 1987) to solve the joint inversion objective function under correspondence map constraints. From equation (1), g is equal to zero in the general case, it is convenient to manipulate it algebraically to avoid the trivial solution, that is when all the coefficients describing the polynomiae are equal to zero. Carrillo and Gallardo (2018) circumvent this problem by normalizing equation (1) by the independent term coefficient a_{00}. The normalized equation (1) becomes

$$\hat{g}(\mathbf{m}_1, \mathbf{m}_2, a) = \sum_{i=0}^{q}\sum_{j=0}^{p} \hat{a}_{ij}\mathbf{m}_1^i\mathbf{m}_2^j = 0, \tag{4}$$

where

$$\hat{a}_{ij} = \frac{a_{ij}}{a_{00}};\ a_{00} \neq 0;\ \hat{a}_{00} = 1. \tag{5}$$

Below is given an example for degree 1, where p and q are equal to 1:

$$\hat{g}(\mathbf{m}_1, \mathbf{m}_2, a) = \hat{a}_{00} + \hat{a}_{01}\mathbf{m}_1^0\mathbf{m}_2^1 + \hat{a}_{10}\mathbf{m}_1^1\mathbf{m}_2^0 + \hat{a}_{11}\mathbf{m}_1^1\mathbf{m}_2^1 = 0. \tag{6}$$

Rearranging and substituting $\hat{a}_{00}$ of equation (5) in equation (6) give

$$\hat{g}(\mathbf{m}_1, \mathbf{m}_2, a) = \hat{a}_{01}\mathbf{m}_1^0\mathbf{m}_2^1 + \hat{a}_{10}\mathbf{m}_1^1\mathbf{m}_2^0 + \hat{a}_{11}\mathbf{m}_1^1\mathbf{m}_2^1 = -1. \tag{7}$$

The joint inversion problem including correspondence maps using Occam's approach is defined as finding the simplest (i.e. smoothest) shear velocity ($\mathbf{m}_1$) and resistivity ($\mathbf{m}_2$) models, which can be correlated by a polynomial relationship and reproduce the observed data. The problem is set to find $\mathbf{m}_1$, $\mathbf{m}_2$ and the normalized coefficients $\hat{a}_{ij}$. Therefore, we propose the objective function as an expanded version of the matrices described in the main equation of Occam, that is

$$\mathbf{m} = [\lambda\partial^T\partial + (\mathbf{WJ})^T\mathbf{WJ}]^{-1}(\mathbf{WJ})^T\mathbf{W}(\mathbf{d} - F[\mathbf{m}_i] + \mathbf{Jm}_i). \tag{8}$$

Here $\mathbf{m}$ is the model parameter to find and $\mathbf{m}_i$ is the model at iteration i, $\lambda\partial^T\partial$ is the smoothing matrix (here the difference in a physical property between consecutive layers); λ is the commonly known Lagrange multiplier, a large λ is a smooth model; $\mathbf{J}$ is the sensitivity matrix, and $\mathbf{d}$ and $F[\mathbf{m}]$ are the observed and calculated data, respectively. $\mathbf{W}$ is the data-weighing matrix, modified from the one in Constable *et al.* (1987) by including a factor F_w, to account for each of the three data types. This factor ensures that a data type with more elements than the others will not inherently bias the inversion. $\mathbf{W}$ is then defined $\mathbf{W} = \text{diag}\,(F_w/\sigma)$, where σ is the uncertainty associated with each data value and F_w:

$$F_w = A_D\frac{N}{N_D}, \tag{9}$$

where A_D is the weight given to data type D with $\sum_{D=1}^{3} A_D = 1$. N_D is the number of data for each type, and $N = \sum_{D=1}^{3} N_D$ is the total number of data. An analysis of the effect of different A_D combinations is presented in Appendix C. Equation (8) is computed over several values of λ in order to find the smoothest model satisfying the misfit:

$$X = ||\mathbf{Wd} - \mathbf{W}F[\mathbf{m}]||. \tag{10}$$

The modified model matrix $\mathbf{m}$ is defined as a matrix that comprises shear velocity, $\mathbf{m}_1$, resistivity, $\mathbf{m}_2$, and the normalized polynomial coefficients, $\hat{a}_{ij}$

$$\mathbf{m} = \begin{pmatrix} \mathbf{m}_1 \\ \mathbf{m}_2 \\ \hat{a} \end{pmatrix}. \tag{11}$$

Similarly, the observed data $\mathbf{d}$ and predicted $F[\mathbf{m}]$ are extended to

$$\mathbf{d} = \begin{pmatrix} \mathbf{d}_1 \\ \mathbf{d}_2 \\ -1 \end{pmatrix}, \tag{12}$$

$$F[\mathbf{m}] = \begin{pmatrix} F_{SWD}[\mathbf{m}_1] \\ F_{MT}[\mathbf{m}_2] \\ \hat{g}[\mathbf{m}_1, \mathbf{m}_2, \hat{a}] \end{pmatrix}, \tag{13}$$

where $\mathbf{J}$ is the general Jacobian matrix that integrates the sensitivity of the given model parameters. More details regarding the Jacobian matrices of the correspondence map function $\hat{g}$ can be found in Carrillo and Gallardo (2018). The complete $\mathbf{J}$ matrix given as the model parameters in equation (11) and data in equation (12) is

$$\mathbf{J} = \begin{pmatrix} \mathbf{J}[\mathbf{m}_1] & 0 & 0 \\ 0 & \mathbf{J}[\mathbf{m}_2] & 0 \\ \mathbf{J}[g_{\mathrm{m}1}] & \mathbf{J}[g_{\mathrm{m}2}] & \mathbf{J}[g_a] \end{pmatrix}. \tag{14}$$

From equation (8), the first term $(\mu \partial^T \partial)$ is related to the smoothness of the model parameters. In our case of joint inversion using correspondence maps, there is no physical or mathematical reason to smooth the coefficients, and hence a smoothness of zero is imposed on the coefficients term. The smoothing term in equation (8) is then as follows:

$$\partial = \begin{pmatrix} \partial \mathbf{m}_1 \\ \partial \mathbf{m}_2 \\ \partial a \end{pmatrix} = \begin{pmatrix} \partial \mathbf{m}_1 \\ \partial \mathbf{m}_2 \\ 0 \end{pmatrix}. \tag{15}$$

The experiments presented in the next section include the retrieval of all model parameters described in equation (11). The aim is to compare separate versus joint inversions for shear velocity and resistivity using the fundamental mode of Rayleigh wave dispersion curves and magnetotelluric data. The workflow followed in all experiments is described in Figure 1.

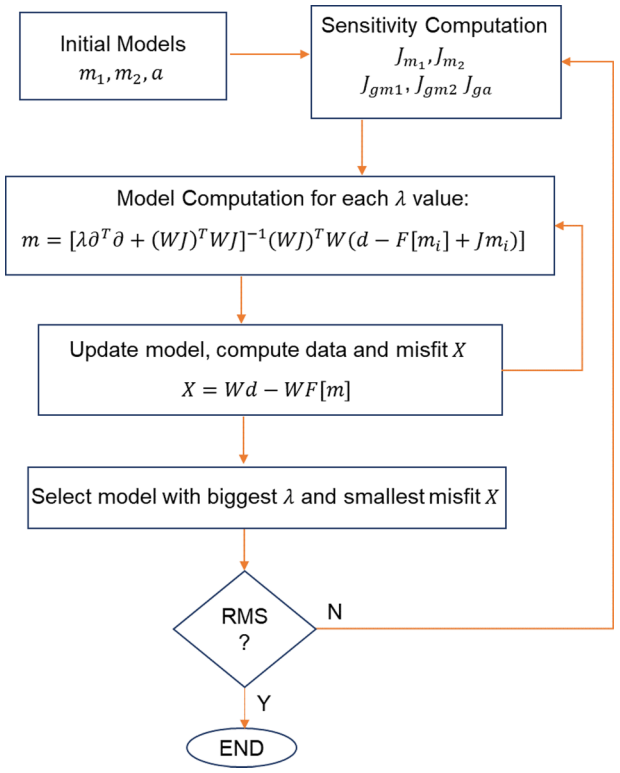

Figure 1 Workflow of joint inversion using correspondence maps; $\mathbf{m}_1$ and $\mathbf{m}_2$ are the log of shear velocity and log of resistivity, respectively.

SYNTHETIC TESTS

To verify the reliability and stability of the inversion algorithm, we test several scenarios of correspondence map relationships using synthetic data: (1) linear relationship, (2) second-order relationship and (3) second-order relationship from well log data. All experiments start with a homogeneous model that does not have to be close to the true model. For the case of the coefficients, the initial model is a vector of ones. The inversions are not constrained by any upper or lower bounds, neither on shear velocity nor resistivity, enabling the correspondence maps to search over a wide range of values. In all experiments, $\mathbf{m}_1 = \ln V_s$ and $\mathbf{m}_2 = \ln \rho$ and 5% random noise is systematically added to the synthetic data. We calculate the synthetic responses for the magnetotelluric (MT) data over logarithmically spaced frequencies between 0.01 and 100 Hz and surface-wave dispersion curves from 0.1 to 10 Hz. The synthetic data are denoted as *Target* in Figures 2, 3 and 7.

Linear relationship: Synthetic test

Although most seismic velocity–resistivity relationships are generally not linear as shown in Carcione *et al.* (2007), we start the joint inversion tests with the most simple scenario

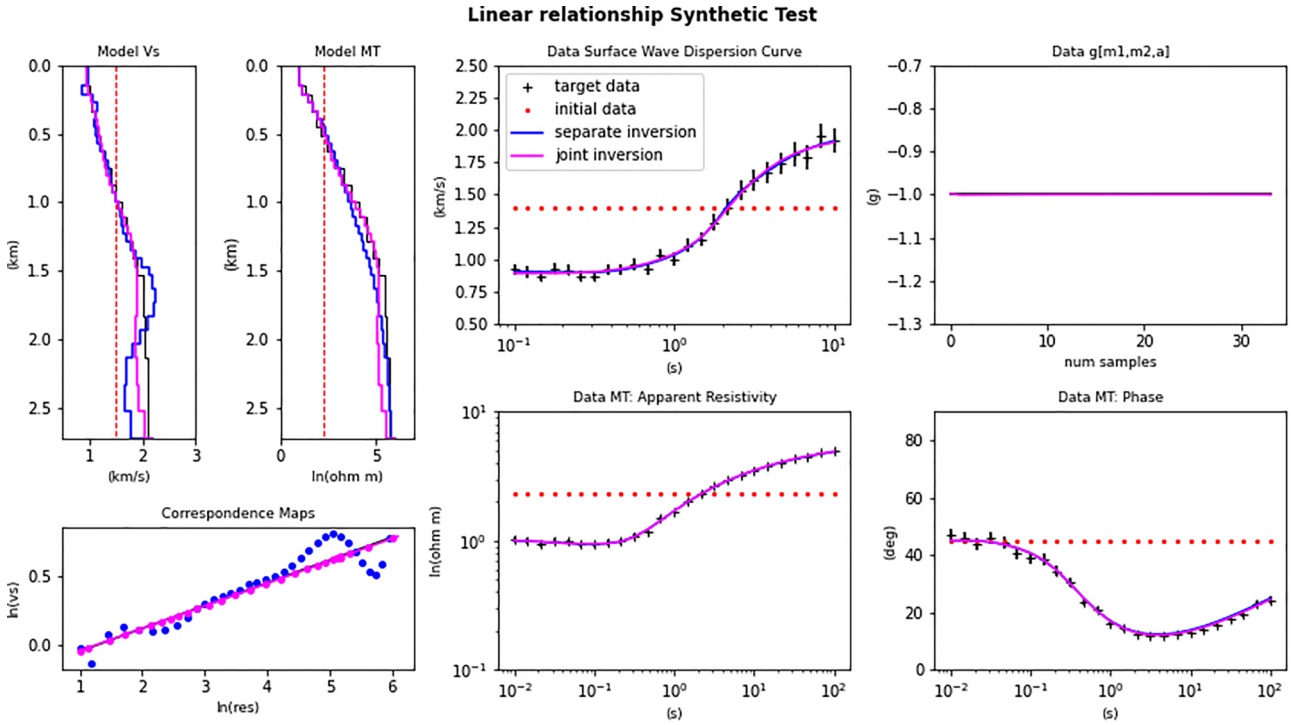

Figure 2 Correspondence map joint inversion results of Section 4.1: shear velocity and resistivity models; synthetic data and models. Colour codes: synthetic (black), starting model (red), separate inversions (*blue*) and joint inversion (*magenta*).

of correspondence map, that is a linear relationship. Linear relationships were observed previously in field data: for example, Harmon *et al.* (2021) recovered linear relationships in the mantle for shear velocity and log resistivity near the Mid-Atlantic Ridge. The cross-plots of these properties, although not true everywhere, show an overall linear trend.

The first experiment consists of a resistivity model ($\mathbf{m}_2$) computed from a set of shear velocity values ($\mathbf{m}_1$) using a linear relationship. The *true* linear relationship from which $\mathbf{m}_2$ is computed for this experiment is

$$\mathbf{m}_2 = 6\mathbf{m}_1 + 1.3. \tag{16}$$

The normalized correspondence map function to search has the form of equation (16), namely,

$$\hat{g}(\mathbf{m}_1, \mathbf{m}_2, a) = \hat{a}_{01}\mathbf{m}_2 + \hat{a}_{10}\mathbf{m}_1 = -1. \tag{17}$$

Figure 2 shows the resulting models and responses from the joint and separate inversions. The shear velocity model from the joint inversion is much closer to the original model, especially below 1 km depth. Sensitivity kernels show that this is the depth (corresponding to periods between 5 and 10 s) from which sensitivity to shear velocity decreases. The correspondence map plots show how the models from the joint inversion align better with the *true* linear relationship than those obtained from separate inversions. The retrieved parameter relationship after 15 iterations is

$$\mathbf{m}_2 = 6.13\mathbf{m}_1 + 1.29, \tag{18}$$

that is very close to the *true* relationship in equation (16).

Non-linear relationship: Synthetic test

The second experiment consists of a resistivity model ($\mathbf{m}_2$) computed from a set of shear velocity values ($\mathbf{m}_1$) using a degree 2 polynomial relationship. This type of relationship has been observed in geothermal environments, where shallow formations dominated by sediments show a decreasing trend in resistivity and an increment towards deeper granitic formations with a persistent increase in the velocity throughout the whole section (Glass *et al.*, 2018), resulting in non-linear parameter relationships. Carcione *et al.* (2007) showed several examples of non-linear relationships between velocity and conductivity in oil-saturated shales and sandstones.

The *true* relationship from which $\mathbf{m}_2$ is computed for this experiment is

$$\mathbf{m}_2 = 26\mathbf{m}_1^2 - 23\mathbf{m}_1 + 6. \tag{19}$$

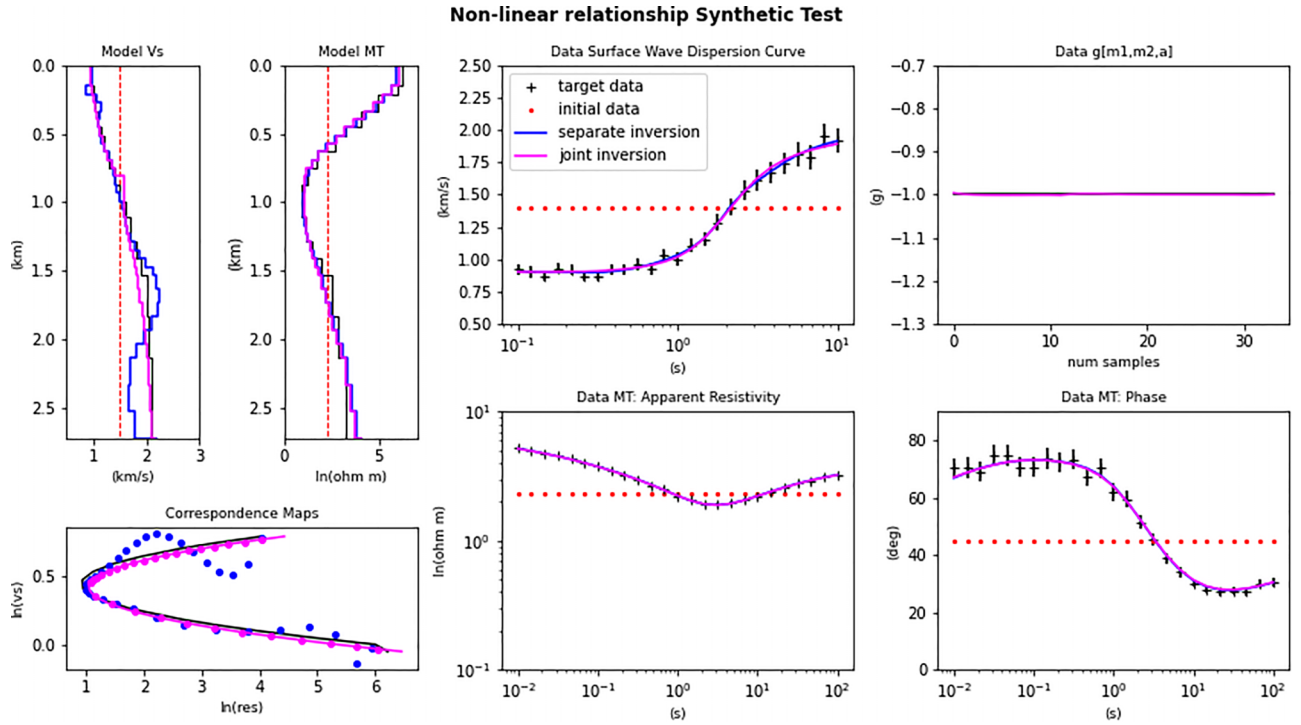

Figure 3 Correspondence map joint inversion results of Section 4.2: shear velocity and resistivity models; synthetic data and models. Colour codes: synthetic (black), starting model (red), separate inversions (*blue*) and joint inversion (*magenta*).

For this experiment, the normalized correspondence map function to search has the following form:

$$\hat{g}(\mathbf{m}_1, \mathbf{m}_2, a) = \hat{a}_{20}\mathbf{m}_1^2 + \hat{a}_{10}\mathbf{m}_1 + \hat{a}_{01}\mathbf{m}_2 = -1. \quad (20)$$

After 15 iterations, the recovered relationship is as follows:

$$\mathbf{m}_2 = 25.7\mathbf{m}_1^2 - 21.5\mathbf{m}_1 + 5.55. \quad (21)$$

The correspondence map plot in Figure 3 shows that the joint inversion (*magenta*) from equation (21) is more consistent with the *true* relationship (black) from equation (19) than the results from separate inversions after 25 iterations (*blue*), which are more scattered, especially for the deeper section of the shear velocity model.

Discussion of linear and non-linear relationships from synthetic tests

To describe how accurate the joint and separate inversions results from the synthetic models are, we assume three factors of the inversion algorithm that are inherently correlated: smoothing, correspondence maps (resulting models) and the data (misfit). In the joint inversion using correspondence maps we are able to retrieve parameter relationships without compromising the smoothing and the data fit.

In Figure 4, we can see how joint inversion results in *magenta* represent a closer shape to the *true* relationship of the models than those of separate inversions for both linear and second degree synthetic tests. In order to quantify how close the correspondence maps obtained from separate and joint inversions was to the true relationships, we compute the $\hat{g}$ function using the pairs of models retrieved from each inversion and compare it to the target $\hat{g} = -1$ within a certain error or tolerance. The green shading in the background represents the $\hat{g}$ value calculated for all ($\mathbf{m}_1$, $\mathbf{m}_2$) pairs in a mesh using the true coefficients. We obtain, for the linear relationship test, that 100% of the joint inversion model pairs (shear velocity–resistivity) have $\hat{g}$ values, computed using the *true* relationship, between −1.05 and −0.95 versus only 15% of the separate inversion pairs. In the non-linear relationship synthetic test, 80% of the joint inversion pairs but 45% of the separate inversion pairs are observed. These joint inversion results lead to a meaningful improvement in the models' relationships without compromising the data fitting. Hence we can say that joint inversion using correspondence maps leads to a reduction in the number of acceptable models that could explain the same observed data ('reduction of non-uniqueness').

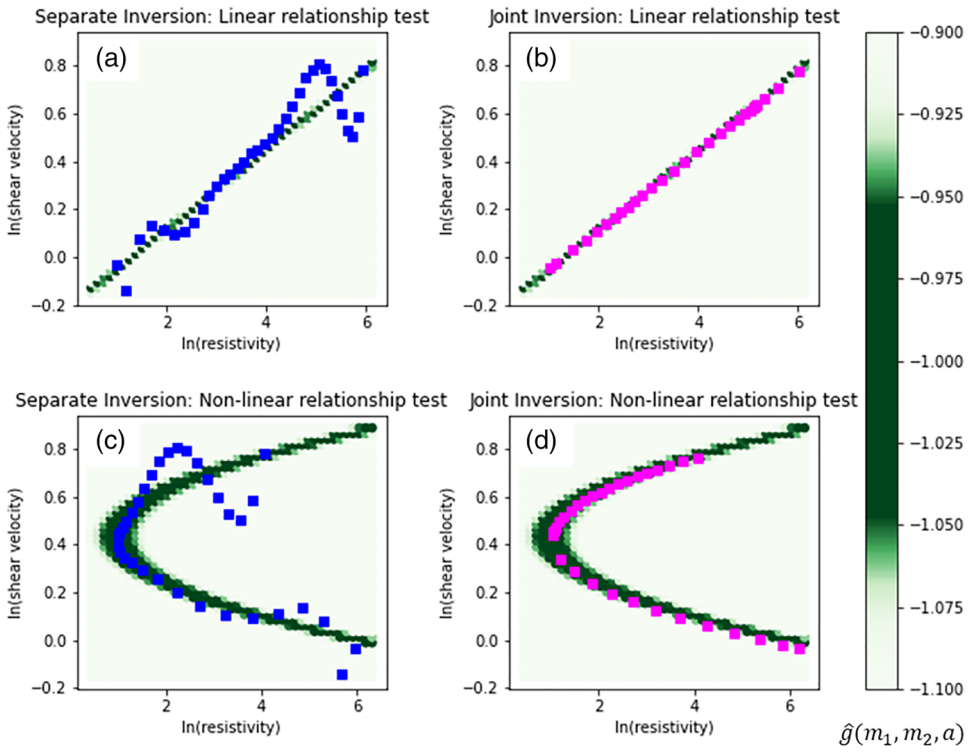

Figure 4 Correspondence map plot for results in Section 4.1 in (a) and b) and for Section 4.2 in (c) and (d). The background mesh in green shading shows the corresponding true relationship $g(\mathbf{m}_1, \mathbf{m}_2, a)$, that is equation (16) for (a) and (b) and equation (19) for (c) and (d), evaluating multiple values of $\mathbf{m}_1$ and $\mathbf{m}_2$. The resulting models for separate (*blue*) and joint inversions (*magenta*) are displayed above. One hundred per cent and 80% of the model pairs in (b) and (d), respectively, have $\hat{g}$ values between −1.05 and −0.95, while only 15% and 45% of the pairs in (a) and (c).

Non-linear relationship: Well log data

The third test consists of a numerical experiment using subsurface parameters extracted from well log data. The first step refers to the problem of defining a proper degree of the polynomial for joint inversion and the second step to the actual results of the joint inversion. The data from well API 15023214760000 were downloaded from the publicly available Kansas Geological Survey database (http://www.kgs.ku.edu/Magellan/Logs/). Among other logs, it includes deep resistivity and compressional slowness logs. For the purpose of this exercise, shear velocity is computed using a constant V_p/V_s ratio of 1.7. Contrary to the previous two experiments, the $\rho - V_s$ relationship here is unknown and hence is closer to a field data case.

Since the correspondence map joint inversion requires the definition of the maximum degree (p and q) in equation (4), the first step is to seek what degree of the correspondence map function is adequate for the joint inversion based on the well log data. For this, we perform an inversion for only the coefficients $\hat{a}_{ij}$ using the well log data (shear velocity and resistivity) and evaluate what type of relationship cover most of the well log physical property pairs.

Four scenarios of coefficient inversions are tested, varying the degree and the terms used in the $\hat{g}(\mathbf{m}_1, \mathbf{m}_2, a)$ function, either the full expression (non-constrained) or a constrained version of the function. The four scenarios of $\hat{g}(\mathbf{m}_1, \mathbf{m}_2, a)$ functions used for testing are described below:

(**a**) Degree 1 non-constrained ($p = 1$ and $q = 1$ in equation (4)),
(**b**) Degree 2 non-constrained ($p = 2$ and $q = 2$ in equation (4)),
(**c**) Degree 1 constrained (equation (17)) and
(**d**) Degree 2 constrained (equation (20)).

By *constrained*, we mean that not all the terms of equation (4) are used, so that $\mathbf{m}_2$ can be expressed as a function of $\mathbf{m}_1$. Therefore, we limit or constrain which terms of equation (4) to be used in the joint inversion problem. Appendix A

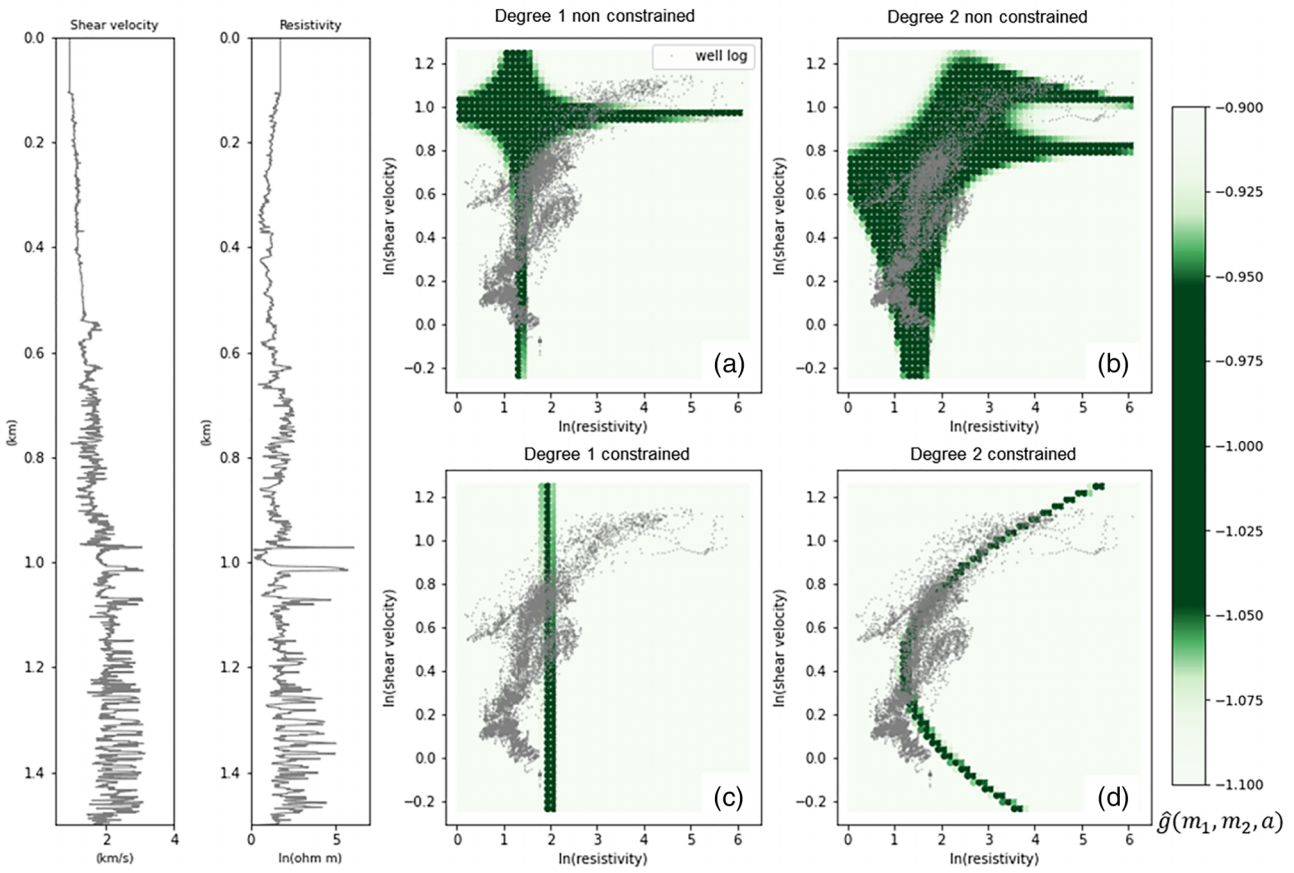

Figure 5 Analysis of degree for correspondence map function on well log data. The left-hand side shows the well log data (grey). The green-shaded background in (a)–(d) shows the evaluated $g(\mathbf{m}_1, \mathbf{m}_2, a)$ functions obtained from separate inversions of the coefficients $\hat{a}$ using degree 1 and 2 (*non-constrained*) and degree 1, degree 2 (*constrained*), respectively. Displayed in all plots are the well log data (grey) for reference. The g functions in the four panels, (a)–(d), were obtained from the separate inversions tests using the well log data (grey).

shows the *constrained* and *non-constrained* form of $\hat{g}$ functions used for this study. On the other hand, *non-constrained* means that the $\hat{g}$ function uses all the terms of equation (4). The results of these four separate inversions of coefficients are displayed in Figure 5. The background colour in each subplot is $\hat{g}(\mathbf{m}_1, \mathbf{m}_2, a)$ evaluated for each $\mathbf{m}_1$ and $\mathbf{m}_2$ pair from a mesh, using the coefficients recovered for the four inversion tests described above.

Figure 5(a,c) shows that more than half of physical property pairs fall outside of the recovered relationships, suggesting that the relationship between shear velocity and resistivity cannot be explained using a linear relationship (degree 1). Therefore, these two scenarios were discarded for the joint inversion.

Although Figure 5(b) covers most of the model parameter pairs, when framed into a joint inversion problem, it can become unstable due to the high number of coefficients to search (i.e. eight for the case of $p = 2$ and $q = 2$). Appendix A, as shown in Figure A.1, exemplifies this subject, which has also been reported in Carrillo and Gallardo (2018). Finally, it is scenario (d) which is used to test the joint inversion strategy since it is the relationship that covers most of the well log model pairs after (b) and explains more closely than (a) and (c) the behaviour of the well log data.

After analysing the degree of polynomial to be used, the second step consists of the actual joint inversion using correspondence maps. For modelling purposes, the well log models are binned into 150 m thick layers to make the computations faster. In Figure 6, it is noted that root mean square (RMS) misfits for the three data types (MT, surface wave dispersion curves and g) marginally decrease after the fifth iteration for the joint inversion test.

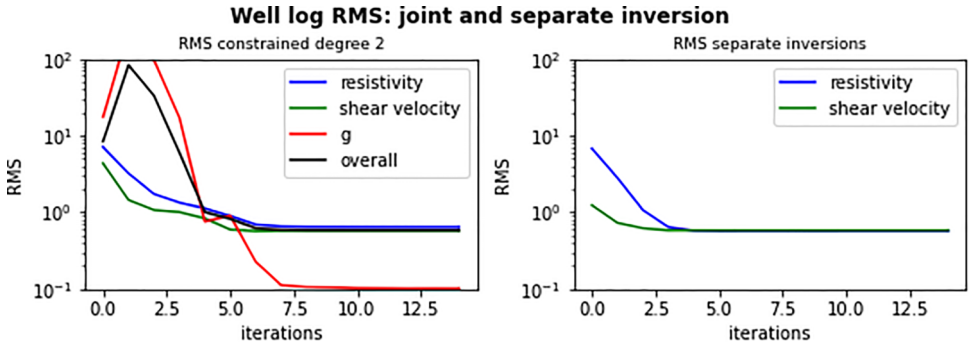

Figure 6 As described in Section 4.4, RMS misfit evolution for joint inversion (left) and separate inversions (right).

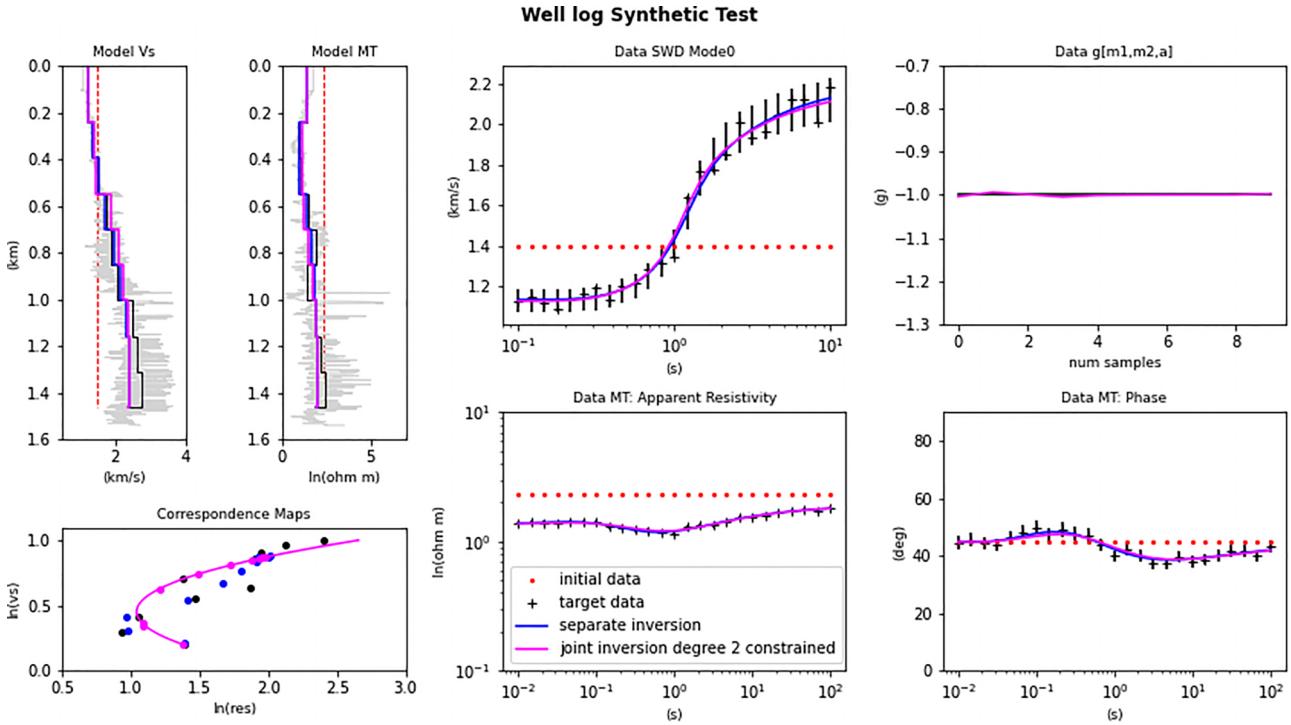

Figure 7 Correspondence map joint inversion results of Section 4.4: shear and resistivity models; synthetic data and model responses. Colour codes: true model (black), starting model (red), separate inversions (*blue*) and joint inversion (*magenta*).

Figure 7 shows that both joint inversion and separate inversion fit the data similarly. From the parameter side, the shallow section represents a model where velocity increases and resistivity decreases, while in the deeper section both properties increase. The joint inversion approach tries to couple these two behaviours as a parabolic form. The recovered relationship for the joint inversion scenario (d) after 15 iterations is as follows:

$$\mathbf{m}_2 = 5.32\mathbf{m}_1^2 - 4.87\mathbf{m}_1 + 2.14. \quad (22)$$

FIELD EXAMPLE

The previous experiments were necessary to assess the reliability of our methodology. As a first application to a real data case, we selected data from northern Alsace, France. This area has historically been explored for hydrocarbons, and more recently hosts the development of deep geothermal systems. A vast amount of geophysical data have been acquired in the region, making it ideal for testing new interpretation and imaging techniques such as the one presented in this paper.

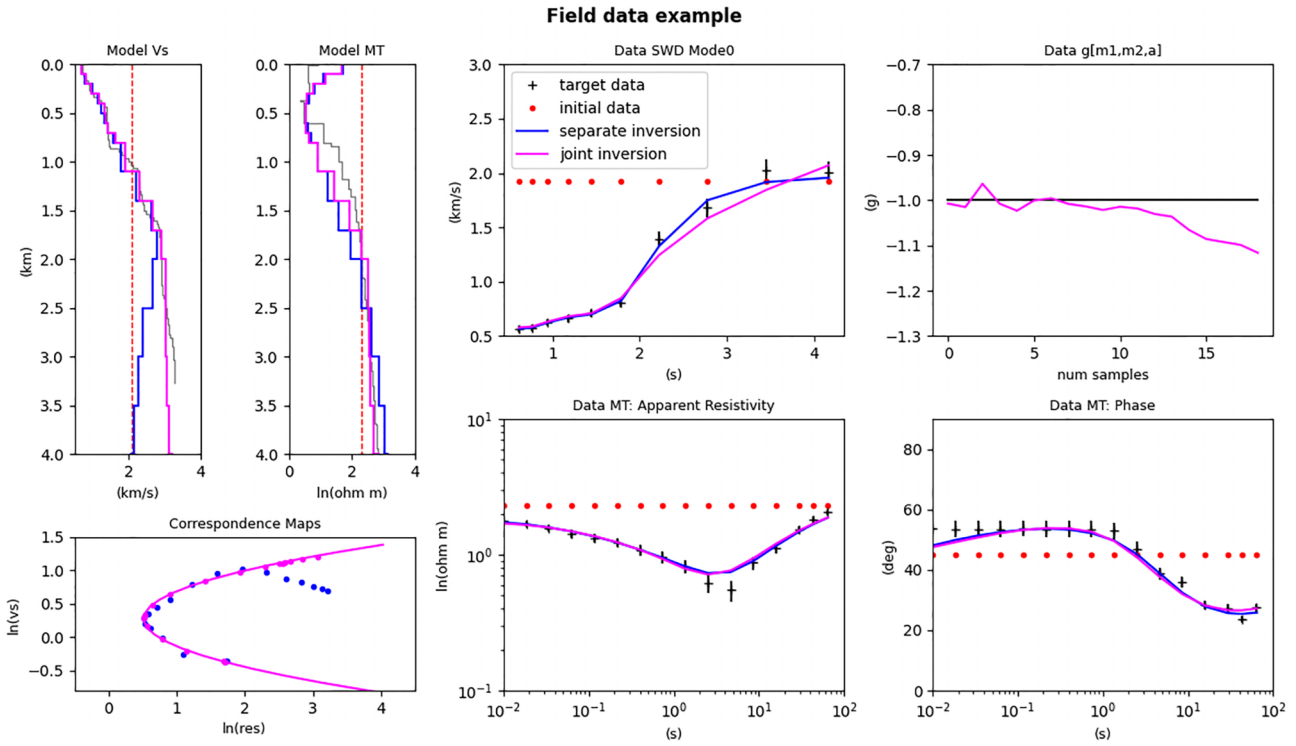

Figure 8 Correspondence map joint inversion results of Section 5: shear velocity and resistivity models; synthetic data and models. Colour codes: reference models (grey), starting model (red), separate inversions (*blue*) and joint inversion (*magenta*).

The datasets tested in this paper consist of one pair of magnetotellurics (MT) sounding from the ECOGI project (Abdelfettah *et al.*, 2019) and fundamental mode Rayleigh wave group dispersion curves from the EstOF network (Lehujeur *et al.*, 2015, 2018). The selected pair of stations (MT-SWD) have a surface separation of at most 150 m. The processed MT data (Abdelfettah *et al.*, 2019) have a frequency range from 0.01 to 100 Hz. The seismological data processed by Lehujeur *et al.* (2015) and Lehujeur (2015) consist of fundamental and first overtone Rayleigh-wave dispersion curves in the range of 0.2–1.28 Hz (0.7–5 s).

Generally, all components of the MT impedance tensor are non-zero and require a three-dimensional modelling approach to be reproduced. Since the scope of this work is one dimensional (1D), we choose an MT station for which the phase tensor ellipse (Caldwell *et al.*, 2004) is closest to a circle over the broad frequency range of interest, that is suitable for our 1D modelling and inversion approach.

A normalized correspondence map function like equation (20) is used for this dataset, since the results from separate inversions (*blue* in Fig. 8) show a parabola in a cross-plot. Models obtained by Abdelfettah *et al.* (2019) and Lehujeur *et al.* (2018) are displayed as reference in grey. Note that the resistivity model from Abdelfettah *et al.* (2019) was obtained from a two-dimensional inversion using MARE2DEM Key (2016), Figure 8 displays the extracted model at the station selected in this joint inversion test. The shear velocity model displayed as reference was obtained from Lehujeur *et al.* (2018), who used a Monte Carlo inversion approach from where the median of the best 2000 models was retained as the solution of the inversion.

The results of the joint inversion (Fig. 8) confirm the use of a non-linear parameter relationship. The introduction of the correspondence map in the joint inversion algorithm results in a shear velocity model below 2.5 km depth closer to the shear velocity model from Lehujeur *et al.* (2018), compared to that obtained by separate inversion. Note, however, that in Lehujeur *et al.* (2018) bounds for shear velocity based on well log data were used as input due to the nature of the Bayesian approach used in their work. In our case, we did not provide any prior information or bounds for shear velocity and resistivity and half-space initial models were used for both parameters. The recovered relationship after 15 iterations was as follows:

$$\mathbf{m}_2 = 2.49\mathbf{m}_1^2 - 1.51\mathbf{m}_1 + 0.81. \tag{23}$$

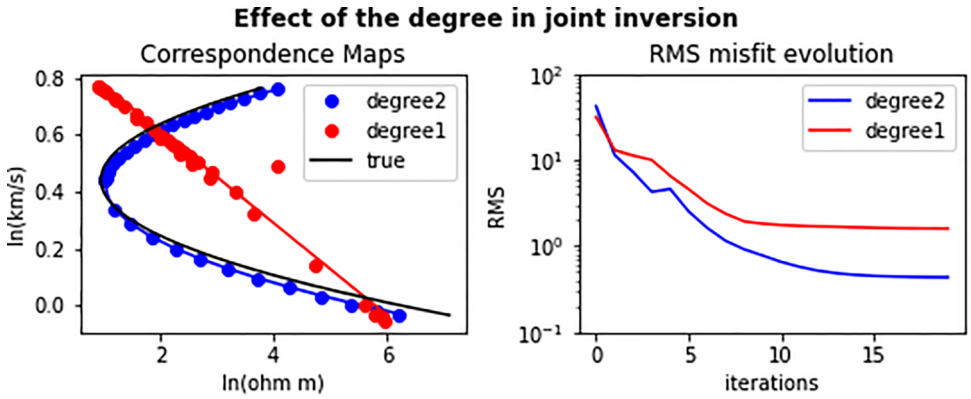

Figure 9 Results of joint inversion of data in Section 4.2 using degree 1 and degree 2, correspondence maps (left) and RMS misfit evolution (right). Non-convergence is observed when performing joint inversion using degree 1.

EFFECT OF THE DEGREE OF $g(\mathbf{m}_1, \mathbf{m}_2, a)$ IN THE JOINT INVERSION

We have seen that the degree of the polynomial relationship used for the joint inversion is an important parameter. Therefore, it is worth investigating how to choose this parameter and how the joint inversion is affected by it. This study started with joint inversions from synthetic models and responses, where predefined relationships were used, that is linear and non-linear. In each of these two synthetic tests, the chosen relationship for the joint inversion was inherently used as the 'correct one', for instance, the non-linear relationship joint inversion used a degree 2 relationship. To study the effect of using different degrees, we took the same synthetic models from Section 4.2 and perform joint inversions using purposely a wrong degree for relationship. That is, for Section 4.2, where the known relationship is non-linear (degree 2), we perform a joint inversion using degree 1. Figure 9 shows the cross-plot ρ-V_s and the root mean square (RMS) evolution at each iteration for this test. We observe that the joint inversion using degree 1 does not converge versus using a degree 2, confirming that the ρ-V_s relationship cannot be explained by a linear function, and therefore a higher order is required. This suggests that when the relationship is unknown, a higher order relationship should be initially tested, followed by decreasing degrees to simplify the solution. If the simpler relationship can explain the data, the joint inversion will converge; otherwise, the higher order relationship must be kept.

As logical approach to decide the degree of joint inversion, one can think of looking at the correspondence maps from separate inversions and use this as a starting point to estimate the degree to use. If we look at the field example in Section 5, both the reference models and the models from separate inversions describe a non-linear relationship and this was the reason why degree 2 was chosen for joint inversion. Appendix B shows the result of the joint inversion for this dataset but using a linear relationship instead. Figure B.1 shows how the fit of the linear relationship joint inversion for the three datasets (dispersion curves, MT: apparent resistivity/phase and $\hat{g}$) is significantly lower than when using degree 2.

CONCLUSIONS

To the best of our knowledge, we have successfully applied a correspondence map joint inversion between surface-wave dispersion curves and magnetotelluric data for the first time. It is an effective way to find meaningful physical parameter relationships while retrieving the shear velocity and resistivity models. The inclusion of correspondence maps in the joint inversion problem has shown to converge without the definition of prior bounds as input and by using homogeneous initial models.

The results of the first two synthetic data examples show how the recovered relationships were essentially the same as the *true* relationships. They also prove that the models retrieved from joint inversion are importantly more similar to the *true* models than those obtained from separate inversions. We observed that when evaluating the $\hat{g}$ function using model pairs from joint and separate inversions, a significantly higher percentage of model pairs from joint inversion had a $\hat{g}$ between -1.05 and -0.95, reducing the number of acceptable models without compromising the data fit ('reduction of non-uniqueness'). The first part of the well log example, the assessment of separate inversions of only the coefficients,

demonstrates an effective way to evaluate and select an appropriate polynomial degree for the joint inversion.

The field data experiment illustrates how joint inversion with correspondence maps achieves a velocity model similar to that obtained by a Bayesian approach (Lehujeur *et al.*, 2018), without forcing boundaries to the model, but rather by imposing the existence of a parameter relationship. It exemplifies how, if a cross-property mathematical correspondence exists that can explain observed apparent resistivity and dispersion curves, the resulting models have a higher coupling than when not using the correspondence map. The addition of a proper correspondence map term has been shown not to compromise the fit of the data in the joint inversion algorithm. It is essential, however, to remind the reader that the convergence of the joint inversion is inherently related to the appropriate selection of the polynomial degree, as described in Section 6.

ACKNOWLEDGEMENTS

We are grateful to CONACyT for awarding a doctoral fellowship to MA. This work was supported by the TelluS Program of CNRS-INSU. Thanks to Jonathan Carrillo and Maximilien Lehujeur for their valuable comments on the implementation of correspondence maps and on the inversion of surface wave dispersion curves, respectively. We also thank two anonymous reviewers for their suggestions that resulted in a largely improved manuscript.

DATA AVAILABILITY STATEMENT

Data sharing not applicable to this article as no datasets were generated or analysed during the current study.

ORCID

M. Aquino https://orcid.org/0000-0002-6623-5107
J. Vergne https://orcid.org/0000-0003-1731-9360

REFERENCES

Abdelfettah, Y., Sailhac, P., Girard, J., Dalmais, E., Maurer, V. and Genter, A. (2019) Resistivity image under grt1-2 geothermal doublet of the Rittershoffen EGS project as revealed by magnetotelluric. In *European Geothermal Congress 2019*, pp. 1–5/ European Geothermal Congress.

Aquino, M., Marquis, G. and Vergne, J. (2021) Joint inversion of magnetotelluric and ambient seismic noise data using correspondence maps. 2021(1), 1–5. https://doi.org/10.3997/2214-4609.202112901

Birch, F. (1960) The velocity of compressional waves in rocks to 10 kilobars: 1. *Journal of Geophysical Research (1896-1977)*, 65(4), 1083–1102.

Caldwell, T.G., Bibby, H.M. and Brown, C. (2004) The magnetotelluric phase tensor. *Geophysical Journal International*, 158(2), 457–469.

Carcione, J.M., Ursin, B. and Nordskag, J.I. (2007) Cross-property relations between electrical conductivity and the seismic velocity of rocks. *Geophysics*, 72(5), E193–E204.

Carrillo, J. and Gallardo, L.A. (2018) Joint two-dimensional inversion of magnetotelluric and gravity data using correspondence maps. *Geophysical Journal International*, 214(2), 1061–1071.

Constable, S.C., Parker, R.L. and Constable, C.G. (1987) Occam's inversion: a practical algorithm for generating smooth models from electromagnetic sounding data. *Geophysics*, 52(3), 289–300.

Dorman, J. and Ewing, M. (1962) Numerical inversion of seismic surface wave dispersion data and crust-mantle structure in the New York-Pennsylvania area. *Journal of Geophysical Research*, 67(13), 5227–5241.

Dufréchou, G., Tiberi, C., Martin, R., Bonvalot, S., Chevrot, S. and Seoane, L. (2018) Deep structure of Pyrenees range (SW Europe) imaged by joint inversion of gravity and teleseismic delay time. *Geophysical Journal International*, 214(1), 282–301.

Gallardo, L.A. and Meju, M.A. (2003) Characterization of heterogeneous near-surface materials by joint 2D inversion of dc resistivity and seismic data. *Geophysical Research Letters*, 30(13), 1658.

Gallardo, L.A. and Meju, M.A. (2004) Joint two-dimensional dc resistivity and seismic travel time inversion with cross-gradients constraints. *Journal of Geophysical Research: Solid Earth*, 109(B3), B03311.

Gautier, S., Tiberi, C., Lopez, M., Foix, O., Lallemand, S., Theunissen, T., Hwang, C. and Chang, E. (2019) Detailed lithospheric structure of an arc-continent collision beneath Taiwan revealed by joint inversion of seismological and gravity data. *Geophysical Journal International*, 218(1), 586–600.

Glass, C., Genter, A., Girard, J.F., Patrier, P. and Vidal, J. (2018) How do the geological and geophysical signatures of permeable fractures in granitic basement evolve after long periods of natural circulation? Insights from the Rittershoffen geothermal wells (France). *Geothermal Energy*, 6, 14.

Haber, E. and Oldenburg, D. (1997) Joint inversion: a structural approach. *Inverse Problems*, 13(1), 63–77.

Harmon, N., Wang, S., Rychert, C.A., Constable, S. and Kendall, J.M. (2021) Shear velocity inversion guided by resistivity structure from the Pi-Lab experiment for integrated estimates of partial melt in the mantle. *Journal of Geophysical Research: Solid Earth*, 126(8), e2021JB022202.

Herrmann, R.B. (2013) Computer programs in seismology: an evolving tool for instruction and research. *Seismological Research Letters*, 84, 1081–1088.

Julià, J., Ammon, C.J., Herrmann, R.B. and Correig, A.M. (2000) Joint inversion of receiver function and surface wave dispersion observations. *Geophysical Journal International*, 143(1), 99–112.

Jupp, D. L.B. and Vozoff, K. (1975) Stable iterative methods for the inversion of geophysical data. *Geophysical Journal of the Royal Astronomical Society*, 42(3), 957–976.

Key, K. (2016) MARE2DEM: a 2-D inversion code for controlled-source electromagnetic and magnetotelluric data. *Geophysical Journal International*, 207(1), 571–588.

Lehujeur, M. (2015) *Imagerie d'un réservoir géothermique par corrélation de bruit*. Ph.D. thesis, Université de Strasbourg.

Lehujeur, M., Vergne, J., Schmittbuhl, J. and Maggi, A. (2015) Characterization of ambient seismic noise near a deep geothermal reservoir and implications for interferometric methods: a case study in Northern Alsace, France. *Geothermal Energy*, 3, 3.

Lehujeur, M., Vergne, J., Schmittbuhl, J., Zigone, D., Le Chenadec, A. and Team, E. (2018) Reservoir imaging using ambient noise correlation from a dense seismic network. *Journal of Geophysical Research: Solid Earth*, 123(8), 6671–6686.

Luu, K. (2019) *Numerical optimization using stochastic evolutionary algorithms : application to seismic tomography inverse problems*. Ph.D. thesis, Mines ParisTech - Université PSL.

Moorkamp, M. (2017) Integrating electromagnetic data with other geophysical observations for enhanced imaging of the earth: a tutorial and review. *Surveys in Geophysics*, 38, 935–962.

Moorkamp, M., Jones, A.G. and Eaton, D.W. (2007) Joint inversion of teleseismic receiver functions and magnetotelluric data using a genetic algorithm: Are seismic velocities and electrical conductivities compatible? *Geophysical Research Letters*, 34(16), L16311.

Ogunbo, J. and Shin, C. (2021) Gramian constraints in electromagnetic multi-physics joint inversion. 2021(1), 1–5. https://doi.org/10.3997/2214-4609.202010366

Shapiro, N.M., Campillo, M., Stehly, L. and Ritzwoller, M.H. (2005) High-resolution surface-wave tomography from ambient seismic noise. *Science*, 307(5715), 1615–1618.

Song, Y., Castagna, J.P., Black, R.A. and Knapp, R.W. (2005) Sensitivity of near-surface shear-wave velocity determination from Rayleigh and Love waves. In: *SEG Technical Program Expanded Abstracts*. Society of Exploration Geophysicists, pp. 509–512.

Tiberi, C., Deschamps, A., Déverchère, J., Petit, C., Perrot, J., Appriou, D., Mordvinova, V., Dugaarma, T., Ulzibaat, M. and Artemiev, A.A. (2008) Asthenospheric imprints on the lithosphere in Central Mongolia and Southern Siberia from a joint inversion of gravity and seismology (MOBAL experiment). *Geophysical Journal International*, 175(3), 1283–1297.

Vozoff, K. (1990) Magnetotellurics: Principles and practice. *Proceedings of the Indian Academy of Sciences - Earth and Planetary Sciences*, 99(4), 441–471.

Ward, S.H. and Hohmann, G.W. (2012) Electromagnetic theory for geophysical applications. In: *Electromagnetic Methods in Applied Geophysics: Volume 1, Theory*. Society of Exploration Geophysicists, pp. 130–311.

Xia, J., Miller, R.D. and Park, C.B. (1999) Estimation of near-surface shear-wave velocity by inversion of rayleigh waves. *Geophysics*, 64(3), 691–700.

Zhang, J. and Morgan, F.D. (1997) Joint seismic and electrical tomography. In: *Conference Proceedings, 10th EEGS Symposium on the Application of Geophysics to Engineering and Environmental Problems*. European Association of Geoscientists and Engineers, pp. 391–396.

Zhdanov, M.S., Gribenko, A. and Wilson, G. (2012) Generalized joint inversion of multimodal geophysical data using gramian constraints. *Geophysical Research Letters*, 39(9), L09301.

APPENDIX A: STABILITY OF CORRESPONDENCE MAP JOINT INVERSION

In order to evaluate the stability of the joint inversion algorithm for a degree 2 using the full expression of $\hat{g}$ ($p = 2$ and $q = 2$), we perform a joint inversion test using the data and model responses from the well log data in Section 4.4. We produce two joint inversion tests: (a) joint inversion using only three coefficients of equation (4), which are described in equation (A.1), and (b) using the full eight coefficients ($p = 2$ and $q = 2$) of equation (4), developed in equation (A.2). The experiments mentioned in this article as *constrained* use the normalized correspondence map function using a limited number of polynomial coefficients, like test (a). On the other hand, the experiments called *non-constrained* use the full expression of the correspondence map function as in equation (4) as in test (b). The $\hat{g}$ functions used in these two joint inversion tests are explicitly described below.

(a) *Constrained* degree 2:

$$\hat{g}(\mathbf{m}_1, \mathbf{m}_2, a) = \hat{a}_{20}\mathbf{m}_1^2 + \hat{a}_{10}\mathbf{m}_1 + \hat{a}_{01}\mathbf{m}_2 = -1 \tag{A.1}$$

(b) *Non-constrained* degree 2:

$$\begin{aligned}\hat{g}(\mathbf{m}_1, \mathbf{m}_2, a) = {} & \hat{a}_{01}\mathbf{m}_2 + \hat{a}_{02}\mathbf{m}_2^2 + \hat{a}_{10}\mathbf{m}_1 + \hat{a}_{11}\mathbf{m}_1\mathbf{m}_2 \\ & + \hat{a}_{12}\mathbf{m}_1\mathbf{m}_2^2 + \hat{a}_{20}\mathbf{m}_1^2 + \hat{a}_{21}\mathbf{m}_1^2\mathbf{m}_2 \\ & + \hat{a}_{22}\mathbf{m}_1^2\mathbf{m}_2^2 = -1\end{aligned} \tag{A.2}$$

The results in Figure A.1 show that the joint inversion can be stable using a restricted number of coefficients, that is the three coefficients in equation (A.1), while it can take more iterations for the non-constrained form to converge or not even converge. For this test, after 15 iterations the non-constrained inversion did not converge to a solution as the constrained inversion did. Carrillo and Gallardo (2018) described instability in the joint inversion of two-dimensional models (gravity and magnetotellurics) when using a large number of coefficients, that is eight coefficients ($p = 2$ and $q = 2$).

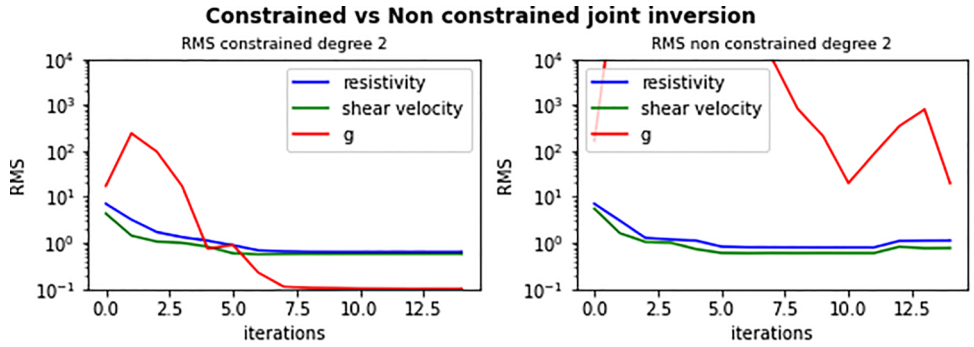

Figure A.1 RMS misfit evolution for constrained (left) and non constrained (right) joint inversion of non-linear relationship test.

APPENDIX B: LINEAR VERSUS NON-LINEAR CORRESPONDENCE MAP JOINT INVERSION IN FIELD DATA

We are also interested in evaluating the influence of the chosen degree of the polynomial relationship (p and q values in equation (4)) on the correspondence map joint inversion. We hence perform two more joint inversion tests on the same field data: (i) correspondence map joint inversion using a maximum degree of 1 (linear relationship) and (ii) degree 2 (parabolic relationship). The parabolic relationship is described in Section 5. It is expected that using a higher order relationship would show better results than including a linear relationship in the joint inversion, since the reference models do not show any hint of linearity.

The results are consistent with our expectations. The linear relationship correspondence map is never able to converge into a solution that can simultaneously fit the data while finding a relationship. This in-

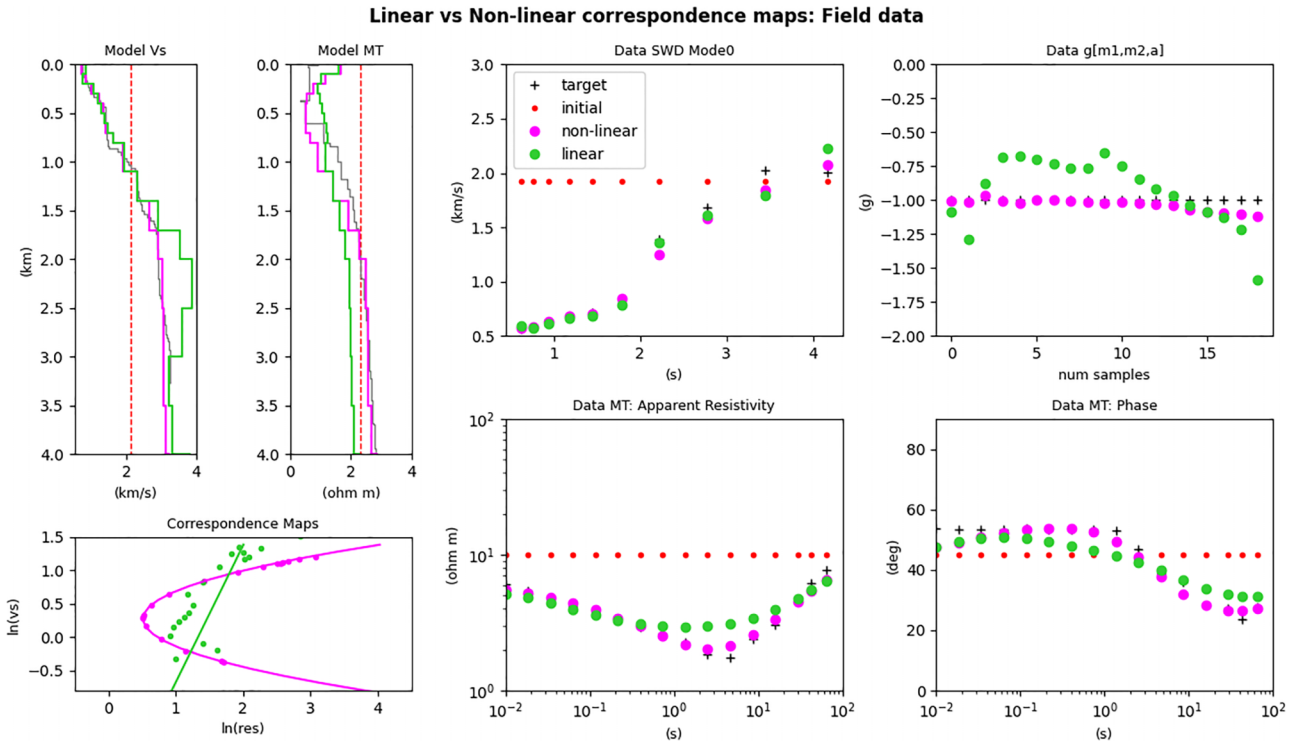

Figure B.1 Correspondence map joint inversion results for data in Section 5 using linear and non-linear relationships. Colour codes: reference models (grey), starting model (red), correspondence map joint inversion using linear relationship (green) and correspondence map joint inversion using non-linear relationship (*magenta*).

Table C.1 Parameters of the tests for weight analysis of joint inversion using correspondence maps

Test	$A_1 = Weight$ (SWD)	$A_2 = Weight$ (MT)	$A_3 = Weight$ (Corr. Map)
(a)	1/3	1/3	1/3
(b)	1/2	1/4	1/4
(c)	1/4	1/2	1/4
(d)	1/2	1/2	0

Abbreviations: Corr. Map: correspondence maps; MT, magnetotelluric; SWD, surface wave dispersion.

dicates that even if the models can be improved via joint inversion using correspondence maps the convergence of the inversion is restricted to a proper selection of the degree of the relationship. The model parameters of this field dataset require a higher polynomial degree in order to fit both observed datasets ($\mathbf{d}_1$ and $\mathbf{d}_1$) while explaining a common relationship as observed in Figure B.1.

APPENDIX C: WEIGHT ANALYSIS OF THE DATA IN THE JOINT INVERSION FRAMEWORK

We investigate the effect of the weight, A in equation (9), of each dataset in the joint inversion framework. Four scenarios of distribution of weights are tested and described in Table C.1. The observed datasets are based on the synthetic datasets of Section 4.2.

The root mean square (RMS) plots in Figure C.1(a–c) show how similar the results of the first three tests are in terms of iterations needed to converge. Figure C.1(d) shows the effect of not giving any weight to the $\hat{g}$ term, which results in a high RMS for this term. Figure C.2 shows the obtained models from these four tests. Overall, the four tests result in very similar models, with the last test showing a slight difference in the correspondence map plot compared to the rest, due to the non-inclusion of the correspondence map term in the joint inversion.

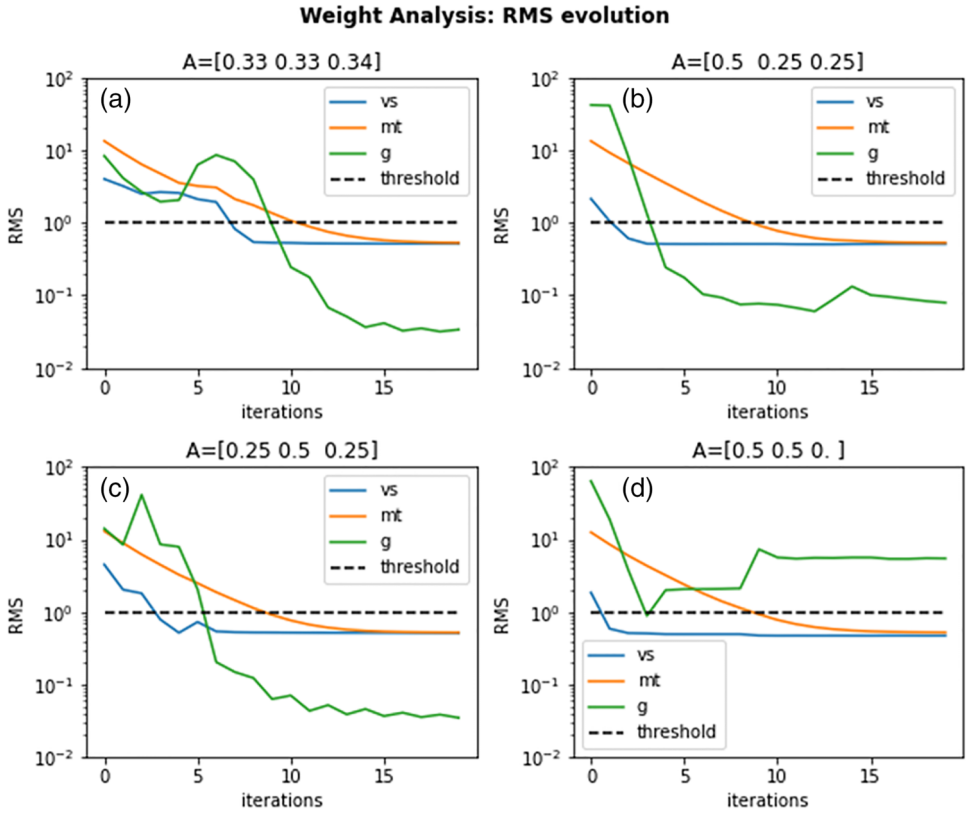

Figure C.1 RMS evolution for the four weight tests described in Table C.1. The dashed black line represents the threshold when RMS = 1. The title of each subplot indicates the value of the weight of each dataset (three values are given), and the order is given as follows: index 1, the weight of the dispersion curve dataset; index 2, the weight of the magnetotelluric dataset; and index 3, the weight of the g dataset.

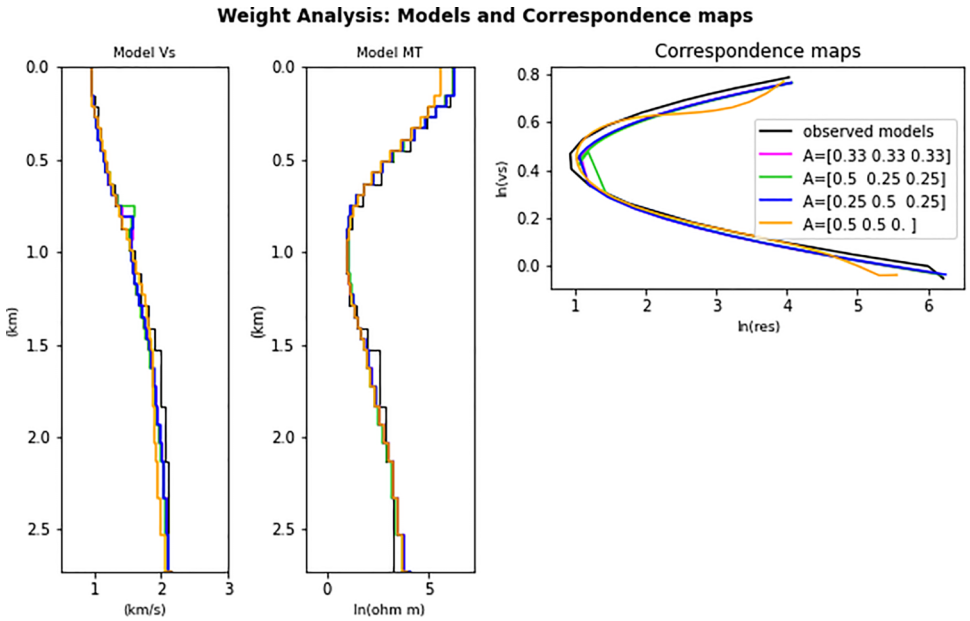

Figure C.2 Resulting models and correspondence maps plots of joint inversion weight tests described in Table C.1. The label of each test indicates the value of the weights of each dataset (three values are given), the order is given as: index 1: weight of dispersion curves dataset, index 2: weight of the magnetotelluric dataset and index 3: weight of *g* dataset In *black* is shown the observed 'true' parameter relationship.

